




Evolution of Microstructure and High-Temperature Tribological Performance of Self-Lubricating Nickel-Based Composite Tungsten Inert Gas Coatings

Suresh Gudala , M.R. Ramesh, and Siva Shanmugam Nallathambi

Submitted: 26 January 2021 / Revised: 20 May 2021 / Accepted: 16 June 2021 / Published online: 9 July 2021

The present study aims to assess the effect of Ag/BaF₂ solid lubricant encapsulation in the nickel-based composite coatings for high-temperature tribological applications. The composite coatings (NiCrSiB/WC and NiCrSiB/WC/Ag/BaF₂) have successfully been fabricated on the titanium 31 substrate by tungsten inert gas (TIG) cladding technique. The influence of the TIG processing current on the microstructure, microhardness, and fracture toughness was investigated. Mechanical characteristics of the coatings were further correlated with the microstructural morphologies. The coating fabricated at 70 A exhibited significantly higher hardness than other coatings. The tribological performances of the NiCrSiB/WC/Ag/BaF₂ composite coatings were superior to those of the NiCrSiB/WC coatings at both low (200 °C) and high (600 °C) temperatures. The synergistic lubrication effect of the Ag/BaF₂ solid lubricant combination provided lubrication at a wide range of temperatures. The addition of these solid lubricants in the nickel-based coating helped achieve the low coefficient of friction of 0.2 and lower wear rates. Particularly, oxide phases (such as NiO, TiO, Ni₃Ti₃O, and W₃O) formed on the worn surface at 600 °C, and the lubricant phases (Ag, Ag₂F, and Ba (TiO₃)) provided excellent resistance to wear.

Keywords high-temperature sliding wear, microstructure, Ni-based composite coating, solid lubricant, TIG cladding

1. Introduction

Titanium and its alloys are widely applied in the fields of aerospace, medical, and automotive industries due to their superior material properties under extreme environmental conditions. Despite higher specific strength, corrosion, and oxidation resistance, titanium alloys exhibit poor wear behavior at higher temperatures. Surface mechanical properties can be improved using several surface modification techniques to extend its application in severe environments (Ref 1). The techniques used to improve the surface properties by adding a composite coating layer include laser cladding (Ref 2), Tungsten inert gas (TIG) cladding (Ref 3), Plasma transferred arc (PTA) cladding (Ref 4), and thermal spray coating (Ref 5).

In many engineering applications, nickel-based alloys were used as the coating material to protect the surface from wear, fatigue, and corrosion (Ref 6). However, nickel-based alloy coatings are not effective without hard ceramic phases such as TiC, WC, SiC, Cr₂C₃, and Al₂O₃ (Ref 7). Among those, tungsten carbide is an extremely hard material that exhibits excellent corrosion and wear properties. It is widely used in

cutting tools, drilling, and preparing corrosion-resistant coatings (Ref 8). Also, ceramic inclusion causes no change in density and other internal properties of the coatings. Hard composite coatings show greater wear resistance. However, they are susceptible to cracking (Ref 9). It is challenging to determine the optimum amount of ceramic phase required to prepare the coating to improve the essential material properties (Ref 10-12). Further, the ceramic phase possesses higher frictional values at elevated temperatures. The subsequent addition of solid lubricant reduces frictional values. Many researchers have used solid lubricants in coatings to enhance the tribological performance. Solid lubricants include soft metals (such as Ag, Pb, and Cu), transition metal dichalcogenides (WS₂, MoS₂, TiS₂, and TaS₂), metal oxides (NiO, MoO₃, and CuO), and alkaline halides (BaF₂, CeF₂, and CaF₂) (Ref 13-19). However, the use of a single solid lubricant cannot provide effective lubrication over a broad temperature range. The use of the low and high-temperature solid lubricant eutectic mixture can improve the tribological characteristics of composite coatings. Torres et al. studied the performance of self-lubricating laser coatings at elevated temperatures and compared the results with those observed for the reference nickel alloy coatings. The results revealed that the composite coating containing lower and higher temperature solid lubricants (Ag and WS₂) effectively lowered the friction and wear at high temperatures (Ref 20). Sahoo et al. revealed that the percentage of CaF₂ presents in the composite TiC-Ni coating affected the value of the coefficient of friction value. As the CaF₂ percentage was increased from 5 to 20%, the coefficient of friction (COF) value decreased from 0.7 to 0.4 (Ref 21). Huang et al. studied the effect of solid lubricant content on the properties of the NiCr/Cr₃C₂ coating. The results revealed that a eutectic content of less than 10% for BaF₂.CaF₂ yielded better tribological performance. It also revealed that the microhardness and tensile strength decreased as the solid lubricant

Suresh Gudala and M.R. Ramesh, Department of Mechanical Engineering, National Institute of Technology Karnataka, Surathkal, India; and Siva Shanmugam Nallathambi, Department of Mechanical Engineering, National Institute of Technology, Tiruchirappalli, India. Contact e-mail: gsuresham@gmail.com.

percentage in the coating increased beyond 10% (Ref 22). Doddamani et al. studied the tribological performance of the composite coating composed of a mixture of CaF₂ and CaSO₄. The results showed an improvement in wear resistance. The reduction in the coefficient of friction was attributed to the lubrication effect exhibited by the coatings (Ref 23). Likewise, hexagonal boron nitride (hBN) exhibited good lubrication properties up to 900 °C because of its graphite-like structure (Ref 24, 25). Lu et al. (Ref 26) reported that an hBN content of 10% in the nickel-based coating showed outstanding performance at 600 °C. Numerous studies have been performed on nickel alloy coatings using thermal spray coating methods. However, the use of the thermal spray coating method leads to increased porosity and poor substrate adhesion. The arc-assisted surface engineering method could be a better alternative to overcome these limitations. The method helps in achieving better metallurgical bonding between the coatings and the substrate. There are very limited studies on the effect of high and low-temperature solid lubricant phases on the tribological performance of the TIG coating at elevated temperatures.

Hence, the present study focuses on the modification of the surface of the titanium 31 alloy substrate with nickel alloy coating containing hard phase reinforcement and lubricating phases using TIG cladding method. Furthermore, the effects of current on the microstructure, microhardness, fracture toughness, grain refinement, and tribological performances were investigated.

2. Experimental Procedure

A grade 31 titanium alloy with a composition of Ti-6Al-3.91V was used as the substrate material procured from Midhani Ltd. India. The commercially available NiCrSiB/WC powder of particle size ranging from 20 to 70 μm was chosen as the base coating material. The chemical composition was reported in wt%: Ni Balance, W 47%, Cr 7.33%, Si 2.21%, Fe 1.91%, B 1.67%, and C 2.37%, and the powder was procured from Hoganas India Ltd. The solid lubricants Ag (10-30 μm) and BaF₂ (10-40 μm) were procured from Alpha Chemica Ltd. The composite powders were prepared proportionately in NiCrSiB/45%WC/5%Ag/10%BaF₂ (wt%) with the help of a tumbler mixer. The rotation was carried out for approximately 24 h.

Figure 1 shows the SEM morphology of the NiCrSiB/WC (coating A) and NiCrSiB/WC/Ag/BaF₂ powders (coating B). The plates of dimension 50 × 50 × 6 mm were cut, and the surface was polished using emery papers and cleaned using acetone to remove any oxide layer or to remove contaminants prior to cladding. The composite powders were mixed with 10% polyvinyl alcohol to make the paste-like solution. The sample was precoated to form a uniform 1 mm-thick layer on the substrate with the help of a metallic sheet. The TIG cladding experiment was conducted using the Fronius Magic Wave 400 machine equipped with a water-cooled head torch. The schematic of the TIG cladding is shown in Fig. 2.

The TIG torch was attached to the CNC table to achieve controllable linear movement. Primary shielding gas flow from the nozzle could protect the instantaneous clad pool, and the

secondary gas flow located behind the torch head was used to protect the clad layer from oxidation. Tadayuki recommended the use of secondary shielding to achieve good welding or cladding in titanium alloys (Ref 27). The generated arc at the torch was used to melt the preplaced powder layer. The experimental process parameters of TIG cladding used in the study are shown in Table 1.

The literature reports revealed that the welding current significantly influenced the energy input. In the present study, processing currents such as 70 A, 80 A, and 90 A were used for fabricating coating A and currents such as 70 A, 75 A, 80 A, 85 A, 90 A, and 95 A were used for coating B. The TIG processing current affects the dilution of the coating with the substrate. The dilution is calculated using the equation suggested by Yaedu and d'Oliveira (Ref 28) as follows:

$$D (\%) = \frac{T_{i\text{coating}} - T_{i\text{powder}}}{T_{i\text{substrate}}} \quad (\text{Eq 1})$$

where $T_{i\text{coating}}$ represents the percentage of the Ti content in the coating, $T_{i\text{powder}}$ is the amount of Ti content in the powder, and $T_{i\text{substrate}}$ is the Ti content in the substrate material. The cross-sectional images of each coating were observed using the scanning electron microscopy (SEM) equipped with energy-dispersive X-ray analysis (EDX). The porosity of the coatings was analyzed using an optical microscope attached to a biovis image analyzer (ARTRAY, AT 130, JAPAN). The microhardness of the coatings was measured using the OMNITECH Vickers microhardness tester, and the indentations were performed on the polished cross section of the sample using a normal load of 300 g. The dwell time was 10 sec. The fracture toughness of the coating is calculated by the following equation proposed by Evans and Wilshaw (Ref 29).

$$K_{IC} = 0.079 \left(\frac{P}{a^{3/2}} \right) \log \left(4.5 \frac{a}{c} \right) \text{ for } 0.6 \leq \frac{c}{a} \leq 4.5 \quad (\text{Eq 2})$$

where P = applied load, a = half indentation diagonal, c = (crack length + half indentation diagonal).

Brittleness refers to the ease with which fractures can propagate within the material. Brittleness is quantified through a parameter known as toughness, which describes the resistance of the material to fracture propagation. The indentations are carried out on the transverse section of the coating with a load of 2000 gf using Vicker's indentation technique. The parameters such as load, crack length, half indentation diagonal are considered for fracture toughness evaluation.

The X-ray diffraction (XRD) studies were conducted on an analytical Empyrean diffractometer with a step size of 0.02°. Grain size distributions in the area fraction and inverse pole figure (IPF) maps were extracted and studied using the EBSD technique.

The high-temperature wear studies were conducted using the pin-on-disk wear machine with alumina (Al₂O₃) disk as a counter surface. During the experiments, the parameters (such as loads of 20 N and 40 N and temperatures of 200, 400, and 600 °C) were varied. The sliding distance was kept constant throughout the experiment. The wear rates were calculated using the weight loss method. The worn surfaces of all the samples were observed and analyzed using the SEM, EDX, and XRD analysis.

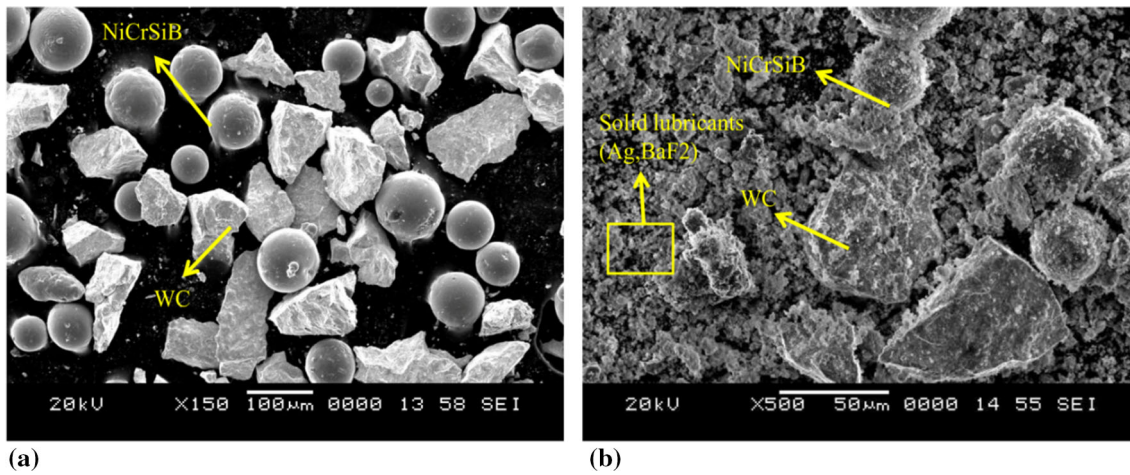


Fig. 1 SEM morphologies of composite powders (a) NiCrSiB/WC and (b) NiCrSiB/WC/Ag/BaF₂

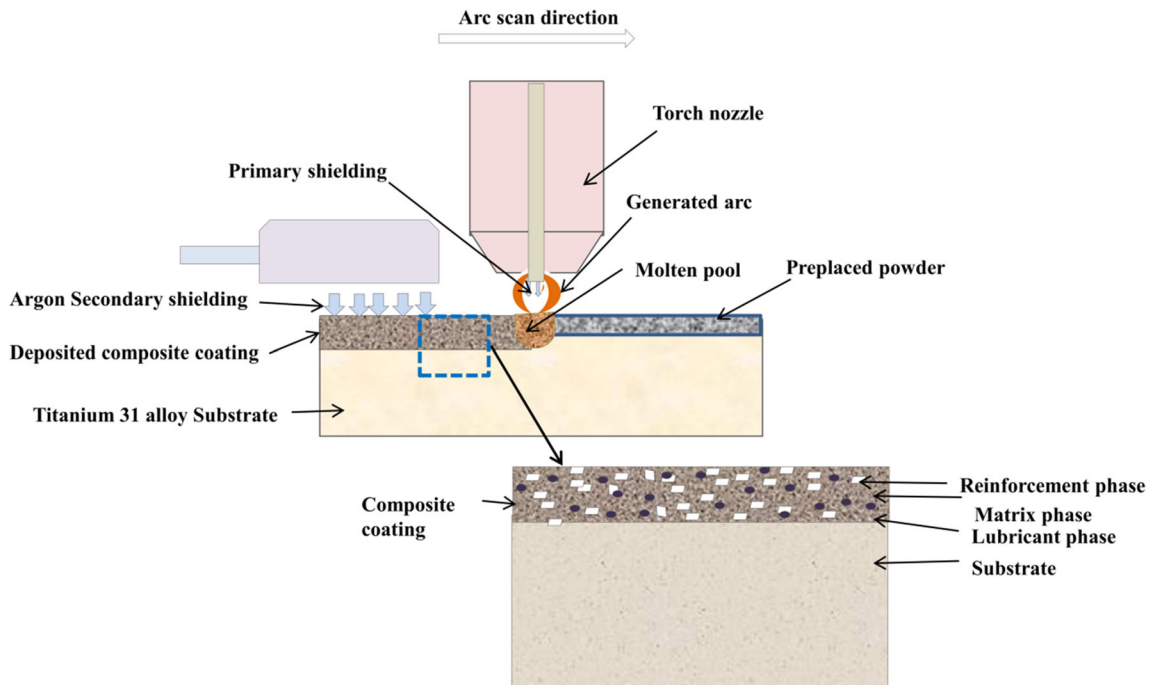


Fig. 2 Schematic representation of the Tungsten inert gas (TIG) cladding experimental setup and mixture of the composite coating

Table 1 TIG cladding experimental processing conditions

Electrode	2 % Thoriated tungsten of diameter 2.4 mm
Current, A	70, 75, 80, 85, 90, 95
Scan speed, mm/s	2
Shielding gas, l/min	Primary 10, Secondary 20 (99.99% pure argon)
Electrode gap, mm	3

3. Results and Discussion

3.1 Microstructure of the Deposited Coatings

The cross-sectional SEM images of coating A and coating B fabricated on titanium 31 substrate are shown in Fig. 3 and 4, respectively. It was observed that coatings A and B were

metallurgically bonded to the substrate. The block-shaped white WC particles were well embedded with the nickel alloy matrix. It was clear that the processing current affected the extent of dilution of the coatings (Ref 30). Dilution impacts the chemical composition and other mechanical properties. Also, the thickness of the coating increased as the welding current increased from 70 A to 95 A. At 70 A, the WC particles did not

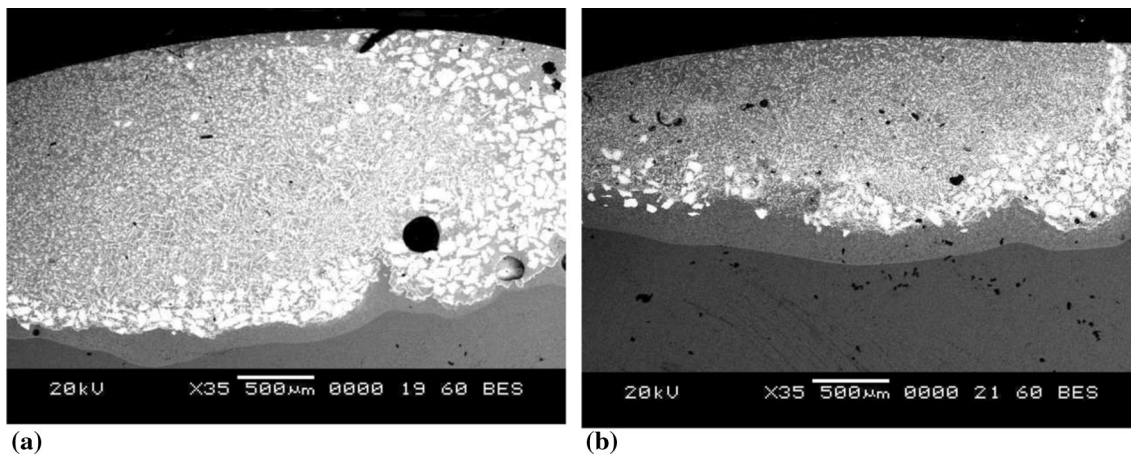


Fig. 3 Cross-sectional SEM images of the coating A produced at the scanning speed of 2 mm/sec at (a) 70 A and (b) 90 A

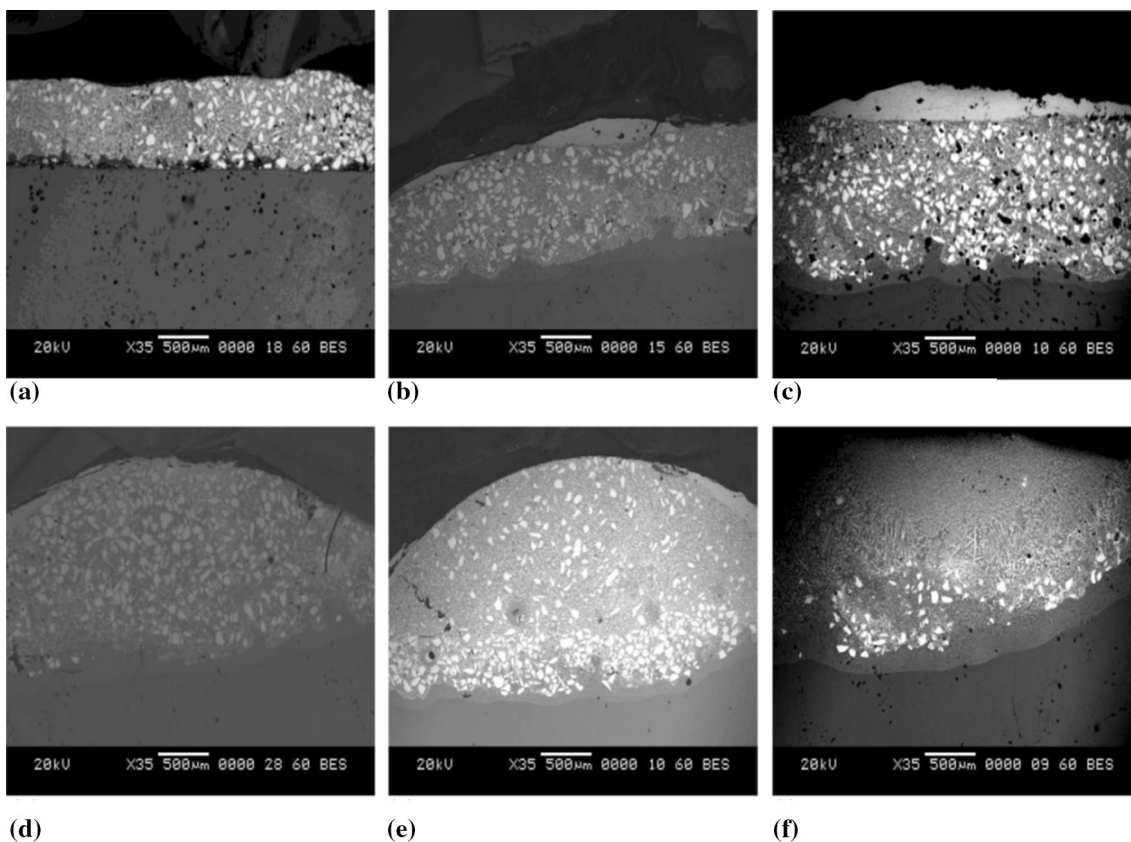
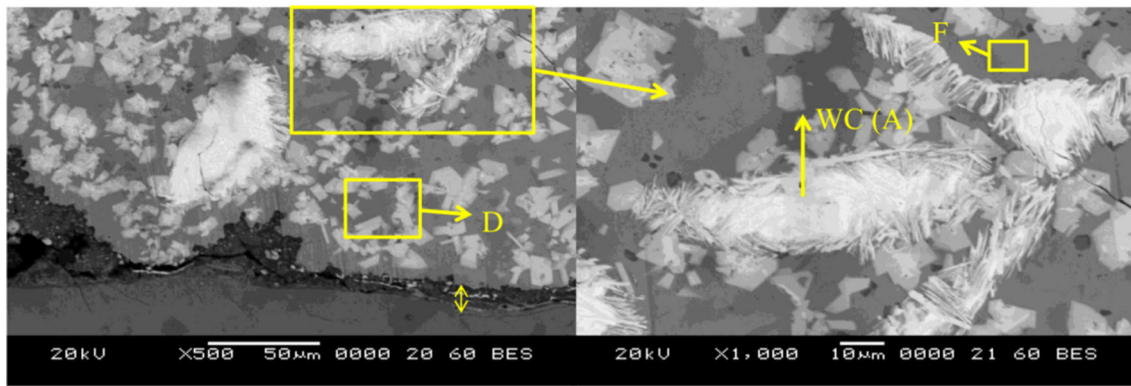


Fig. 4 Cross-sectional SEM images of the coating B produced at the scanning speed of 2 mm/sec at (a) 70 A, (b) 75 A, (c) 80 A, (d) 85 A, (e) 90 A, and (f) 95 A

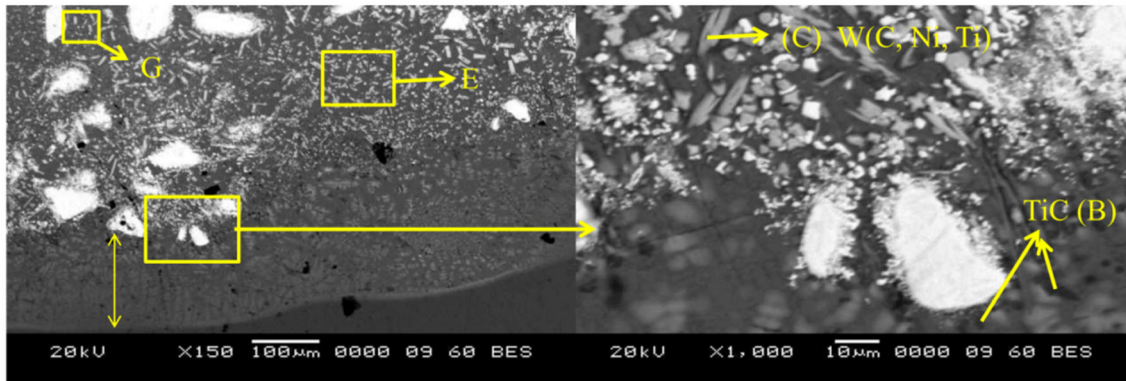
fully dissolve in the nickel matrix. At 95 A, WC particles are well dissolved. The dissolution could be attributed to their high fusion temperature. The residual WC particles were collected at the bottom of the coating. This can be potentially attributed to the higher density and melting point of the WC particles. The weld pool convection current was not high enough to prevent the WC particles from sinking to the bottom (Ref 31).

It was observed that micro-cracks and few pores were present in the coating. The thermal stresses induced in the coating induced cracking because of the high thermal gradient (Ref 32). The heat input and cooling rate affected the porosity

content of the coating. The average percentage of porosity was recorded to be less than 2%. The thermal gradient significantly affected the porosity. A decrease in porosity was observed as the heat input increased. Figure 5 shows the magnified SEM images of coatings at 70 A and 95 A. As welding current has greater significance and correlation for generating heat input, comparatively high dilution was observed when the welding current was 95 A (17.18%) than when it was 70 A (5.92%). It can be seen that the 95 A processed coating had a high concentration of Ti (shown in Table 2) near the interface (region E). The depths of the interface region of coating B at 70



(a)



(b)

Fig. 5 Magnified cross-sectional SEM morphology of the coating B (a) near the interface at 70 A and (b) near the interface at 95 A

Table 2 EDX analysis at different areas as marked in Fig. 5 of coating B

Region	Ni	Cr	Fe	Si	B	W	C	Ti	Al	V	Ag	Ba	F
A	3.28	0.82	1.42	3.35	2.05	66.99	18.32	0.08	1.03	0.02	0.84	1.70	0.10
B	3.69	1.10	2.34	0.39	0.26	4.82	17.71	64.65	1.82	1.49	0.47	1.2	0.06
C	13.87	3.28	1.01	2.34	2.53	30.24	13.92	25.16	1.84	1.37	0.43	4.0	0.01
D	55.90	7.30	2.25	2.91	0.81	16.66	5.34	6.19	0.60	0.02	0.52	1.09	0.41
E	16.68	3.00	1.01	1.65	0.28	15.26	3.55	49.28	3.68	2.11	0.55	2.70	0.25
F	59.76	9.47	2.29	3.48	1.06	7.15	13.83	0.18	0.44	0.01	0.74	1.24	0.36
G	37.67	6.95	1.93	3.66	1.46	10.69	15.90	15.50	1.40	0.44	0.78	3.34	0.28

A, 80 A, 90 A, and 95 A are 85 μm , 105 μm , 128 μm , and 169 μm , respectively. It is worth noting that the substrate thermal conductivity and coating process parameters primarily affect the diffusion behavior (Ref 30). The processing current changes the degree of dissolution of the WC particles. At lower heat input, flower-shaped WC particles were observed near the interface. With the increase in the current, the degree of dissolution was low, and blocky WC particles were found to concentrate near the interface. The difference in their appearance could be attributed to the change in the thermal gradient.

The EDX results at different regions marked in Fig. 5 are tabulated in Table 2. Analysis of the EDX results revealed that the white granular phase was rich in W and C. The dark dendritic phases were rich in Ti and C, and light gray particles were primarily composed of W, Ti, C, and Ni. The area D was primarily composed of Ni and W and included the limited

percentage of Ag, Ba, F, C, Ti, Cr, Fe, and Si. The area E (near the interface at 95 A) contained a higher amount of Ti due to the dilution effect. The area F was primarily composed of nickel and a small percentage of other elements such as C, Ti, W, Ag, Ba, and F. It is regarded as the nickel alloy matrix. Darker dendritic and gray phases were observed in the coatings at 95 A compared to 70 A, which could be attributed to the higher concentration of TiC and TiNi phases in the coating. Matrix, reinforcement, and lubricant phases were well dispersed in the coating, as shown in EDX elemental mapping (Fig. 6).

Silver has low mixing enthalpy with the nickel alloy, which leads to the formation of separate precipitates during the coating development (Ref 20). Ag precipitates were observed in the elemental map. However, the high-temperature solid lubricant BaF_2 fully dissolved in the coating instead of forming

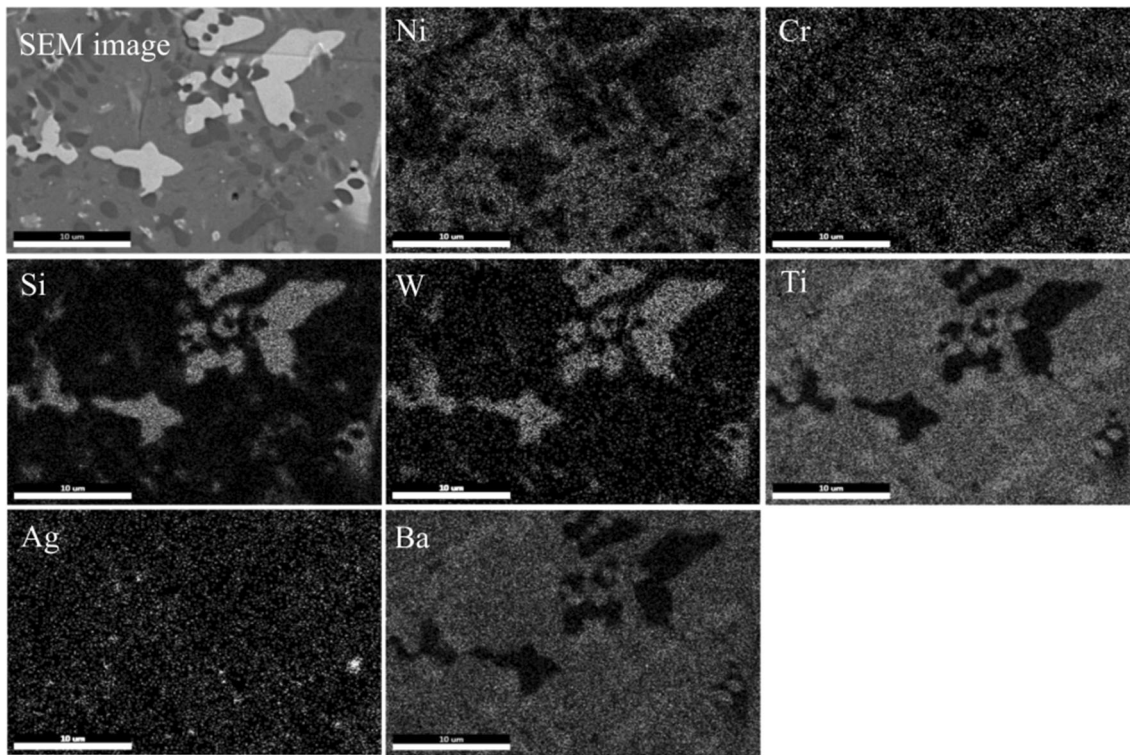


Fig. 6 EDX elemental mapping of coating B across the cross-section (near the surface) at 70 A

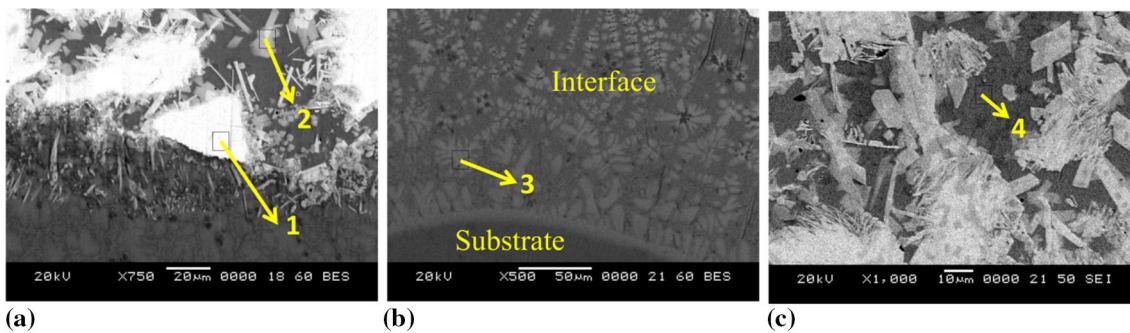


Fig. 7 SEM image of coating A processed at 70 A. (a) Just above the coating-substrate interface, (b) at the coating-substrate interface, and (c) coating region

a separate phase. But fluoride was not quantified accurately. Light elements such as B, F, and H were difficult to quantify using the EDX analysis (Ref 33).

Figure 7 represents the magnified cross-sectional images of the TIG clad deposited when the current was 80 A. It could be seen that coating A was metallurgically bonded to the substrate. Figure 7(a) shows blocky white shaded particles (region 1) rich in W and C. The gray-shaded particles (region 2) primarily contained W and Ni (Table 3). Near the interface, interdendritic eutectic precipitations were found, as seen in Fig. 7(b). The dendritic structure formed on the substrate grew toward the clad layer. These dendritic structures at the interface (region 3) were rich in titanium and nickel (Table 3), and the matrix (region 4) consisted of a nickel alloy.

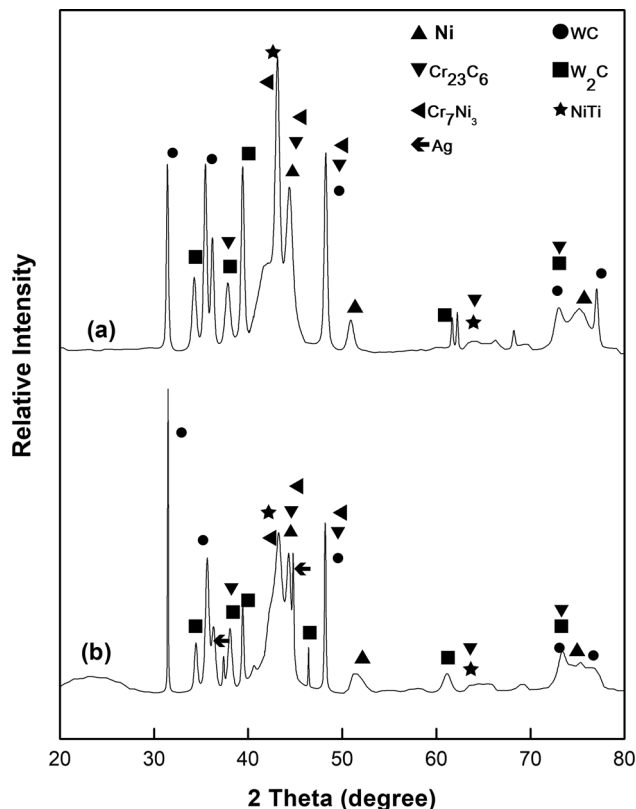
Figure 8 shows the XRD patterns of the coatings A and B processed at 70 A. It was evident that the coatings primarily consisted of Ni, Cr_{23}C_6 , Cr_7Ni_3 , WC, W_2C , and NiTi. Oxides were absent in the coatings because of the primary and

secondary shielding argon protection achieved during the process of fabrication. WC dissolution was observed in the coating due to the higher heat input, resulting in the formation of W_2C . The coating was mixed with titanium due to the higher energy input, which caused the formation of the intermetallic NiTi compound. The presence of Ag indicates the synergistic lubrication effect in the coating.

Figure 9(a-c) shows the EBSD IQ, grain distribution, and IPF map of coating B fabricated at 70 A. It consisted of Cr_7Ni_3 (orange), Cr_{23}C_6 (yellow), NiTi (Blue), W (Pink), and silver (red). The unindexed regions are shown in black in Fig. 9(b, g). The analysis of the figures indicates that the coating is composed of blocky grains. The amount of heat input and cooling rate influences the extent of grain refinement in the clad (Ref 34). It further influences the mechanical characteristics of the coating (Ref 35). The grain size was found to be in the range of 0.1-10 μm , and the average grain size was 4 μm . Solute redistribution occurred during the solidification of the

Table 3 Elemental distribution of the selected regions of coating A as marked in Fig. 9

Region	Ni	Cr	Fe	Si	B	W	C	Ti	Al	V
1	2.25	1.09	0.85	4.47	1.54	76.32	10.84	0.79	1.25	0.60
2	19.46	3.62	1.90	2.72	3.21	52.37	14.33	0.96	0.83	0.58
3	12.05	2.62	1.54	0.86	0.17	5.88	3.02	65.14	5.47	3.25
4	61.15	8.74	5.90	3.34	1.63	4.67	13.15	0.68	0.45	0.29

**Fig. 8** XRD patterns of the coatings at processing current of 70 A. (a) Coating A and (b) coating B

alloy coating. The results indicated that the Cr_7Ni_3 and Cr_{23}C_6 were present as the primary phases, and they were present in 53.3 and 22.8%, respectively (Fig. 9c). Solid lubricants Ag and BaF_2 are not quantified accurately. The elements, with a distribution coefficient (k) greater than 1 (Ni, Cr, and Fe), diffuse into the dendrite regions during solidification of the clad (Ref 36). Usually, eutectic products exhibiting a low melting point form between the dendrites. Analysis of Fig. 9(e, h) revealed that the clad was primarily characterized by a few blocky and elongated equiaxed grains. The reduction in the grain size could be attributed to the increase in the heat input and change in thermal gradient (Fig. 9h). The grain size at 95 A was in the range of 0.01–8 μm , and the average grain size was 2 μm . The phases obtained by the EBSD maps were consistent with the XRD and EDX results.

3.2 Microhardness

Figure 10 represents the microhardness profile of the coating B fabricated at 70 A, 80 A, 90 A, and 95 A. The indentations were performed along the cross-section using the Vickers

hardness tester throughout the coating depth. As the current increased from 70 A to 95 A, a reduction in the microhardness was observed. Also, it was noted that the coating surface exhibited a higher hardness value. A gradual reduction in the hardness value was observed as moved toward the interface. Due to the collected WC particles at the bottom, there was a sudden increment in the microhardness. The microhardness values of the bulk composite coating B were varied from 1500 $\text{HV}_{0.3}$ to 650 $\text{HV}_{0.3}$, which is about 2.03–4.68 times as that of the titanium 31 substrate (approximately 320 $\text{HV}_{0.3}$). The phases such as Cr_{23}C_6 , WC, W_2C , and Cr_7Ni_3 were primarily responsible for the high hardness. The microhardness values suddenly changed for the 70 A processed coatings near the interface. This could be attributed to the comparatively less extent of dilution in the presence of the substrate. The coating deposited at a higher processing current of 95 A exhibited a gradual reduction in the microhardness at the interface due to significant dilution. The average microhardness values of coating A were higher than that of coating B due to the higher percentage of the ceramic inclusion. The process current was increased from 70 A to 95 A. The average microhardness values of the coatings were found in the range of 725–848 $\text{HV}_{0.3}$. The average microhardness values of coating B were in the range of 668–830 $\text{HV}_{0.3}$. It was clear that the 15% encapsulation of the solid lubricant phase in coating B resulted in a reduction in the hardness value. Figure 11 shows the average microhardness values of coating A and coating B at 70A. The higher percentage of ceramic inclusion in coating A is mainly responsible for higher microhardness values. It is evident that the average hardness values are gradually decreased from clad surface to the interface.

3.3 Fracture Toughness and Interfacial Strength

Figure 12 shows the indentation of load 2000 gf on the cross-sectioned sample. The fracture toughness values of the coating B at 70 A, 75 A, 80 A, 85 A, 90 A, and 95 A were 3.85, 4.06, 4.28, 5.12, 5.68, and 6.01 $\text{Mpa}\cdot\text{m}^{0.5}$, respectively. The ceramic phase in the coating caused the cracks at 2000 gf. Indentations were performed along the interface to measure the interfacial strength of the substrate coating. There was no apparent damage observed on the interface as the load increased from 500 to 2000 gf. The results revealed that the coatings deposited under conditions of higher processing current exhibited better fracture toughness compared to the other processed coatings developed under conditions of varying currents.

3.4 High-Temperature Tribological Performance of Coatings

The tribological performances of the coatings were evaluated using a pin-on-disk tribometer under dry sliding conditions. The properties related to tribological performance are not

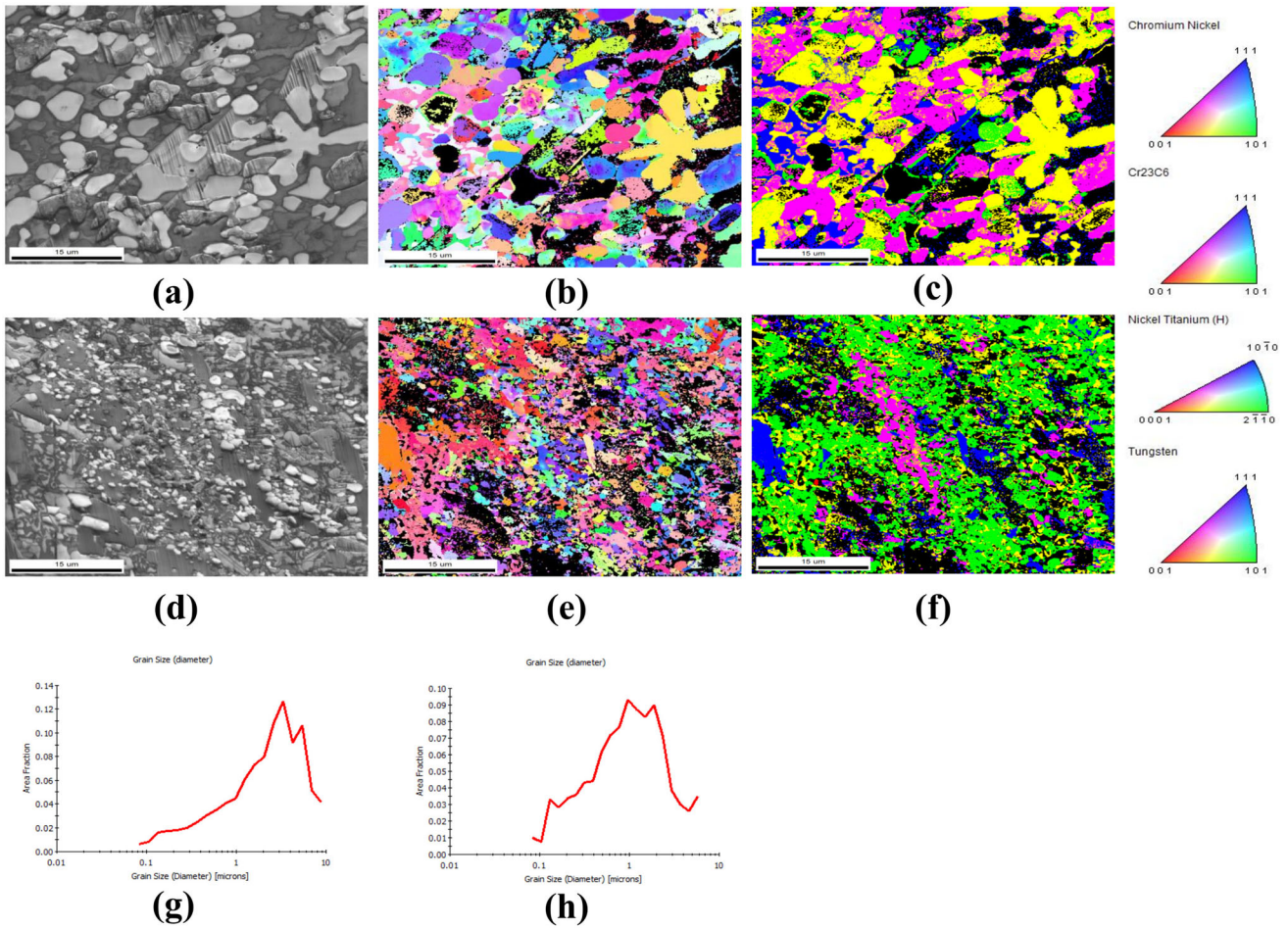


Fig. 9 EBSD IPF maps and grain distribution of the coating B along the cross-section. (a) IQ map at 70 A and (b) grain size distribution map at 70 A. (c) IPF map at 70 A, (d) IQ map at 95 A, (e) grain size distribution map at 95 A (f) IPF map at 95 A (g) grain size distribution in the fractioned area at 70 A and (h) grain size distribution in the fractioned area at 95 A

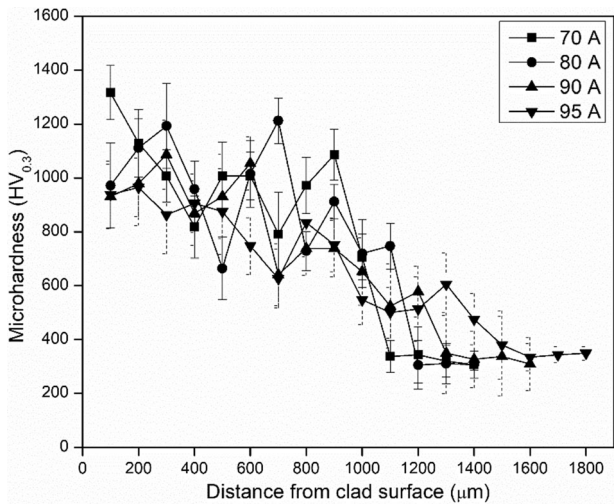


Fig. 10 Microhardness profile of the coating B at the coating cross-section for various TIG currents

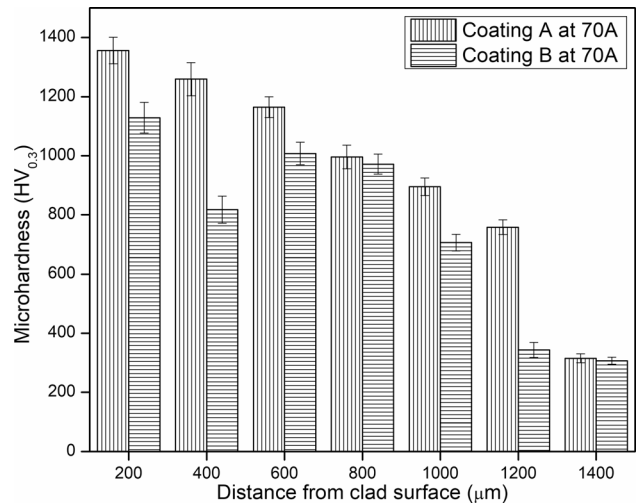


Fig. 11 Variation of average microhardness values of coating A and coating B at 70A

intrinsic but rely on factors such as load, temperature, atmospheric conditions, and sliding speed. The TIG clad samples produced at 70 A processing current exhibited the highest microhardness. The effect of temperature and load on

the tribological performance was also studied. Figure 13 exhibits the weight loss of coatings A and B under the load of 20 N and 40 N. The temperatures were varied as 200 °C, 400 °C, and 600 °C. In the sliding wear operation, tribology

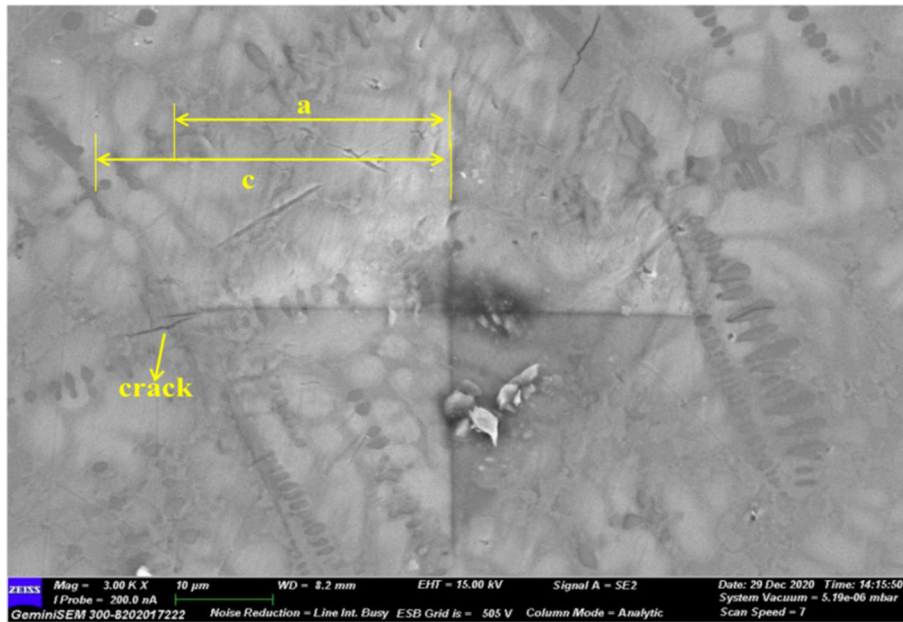


Fig. 12 SEM image of indentation mark and crack observed during the evaluation of fracture toughness of coating B

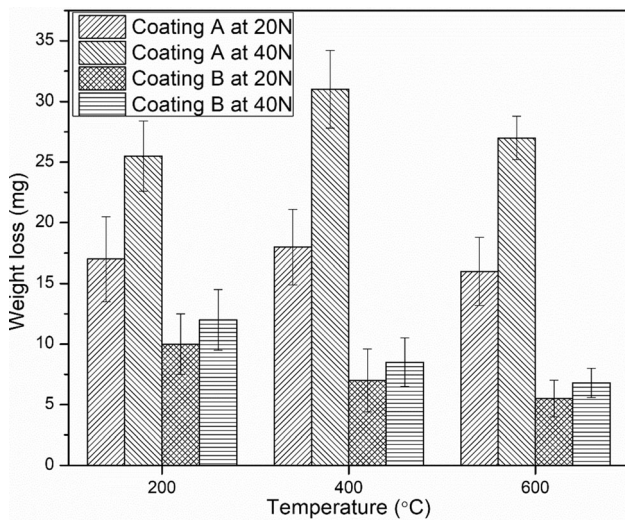


Fig. 13 Variation of weight loss of coating A and coating B at varying temperatures and loads

chemical interactions of the coatings with the counter body under an operating environment can be observed. These induce local temperatures and shear stresses along the contact zones (Ref 37). As shown in the bar chart, the weight loss of the coating A increased from 17 to 25 mg at 200 °C when the loads were varied from 20 to 40 N. The increase in the load to 40 N resulted in material removal against the counter body. The weight loss increased from 10 to 13 mg for the coating B when the load was increased from 20 to 40 N at 200 °C. The weight loss of the coating B samples decreased with an increase in the temperature from 200 to 600 °C. This was attributed to the formation of the tribo layer on the coating surface. It was observed that the weight loss was higher at 400 °C, when the load was 40 N for coating A. The coating B showed higher weight loss at 200 °C when the load was 40 N. However, coating B performed well at both lower (200 °C) and higher

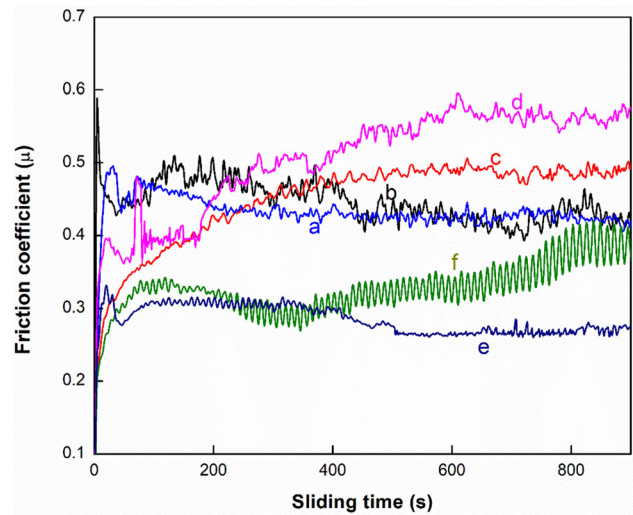


Fig. 14 Variation in the coefficient of friction with respect to the sliding time for Titanium 31 at (a) 200 °C and (b) 600 °C, (c) coating A at 200 °C and (d) 600 °C, (e) coating B at 200 °C and (f) 600 °C

(600 °C) testing temperatures. At 600 °C, both solid lubricants Ag and BaF₂ remained active. The weight loss was further reduced to 4 mg when the load was 20 N. The weight loss of the titanium 31 substrate is increased with the increase in load as well as temperature. At 20N load and 200 °C, weight loss is found to be 250 mg. With the increase in temperature from 200 to 400 °C, weight loss was increased to 270 mg. Further, weight loss was increased to 350 mg at 600 °C. Similarly, weight loss was increased from 360 to 570 mg at 40N load with the rise in temperature (200-600 °C).

Several factors such as porosity, properties of partially melted particles, wear debris, and polished sample surface create uncertainty in the wear properties. No significant change was observed in weight loss, and coefficient of friction when

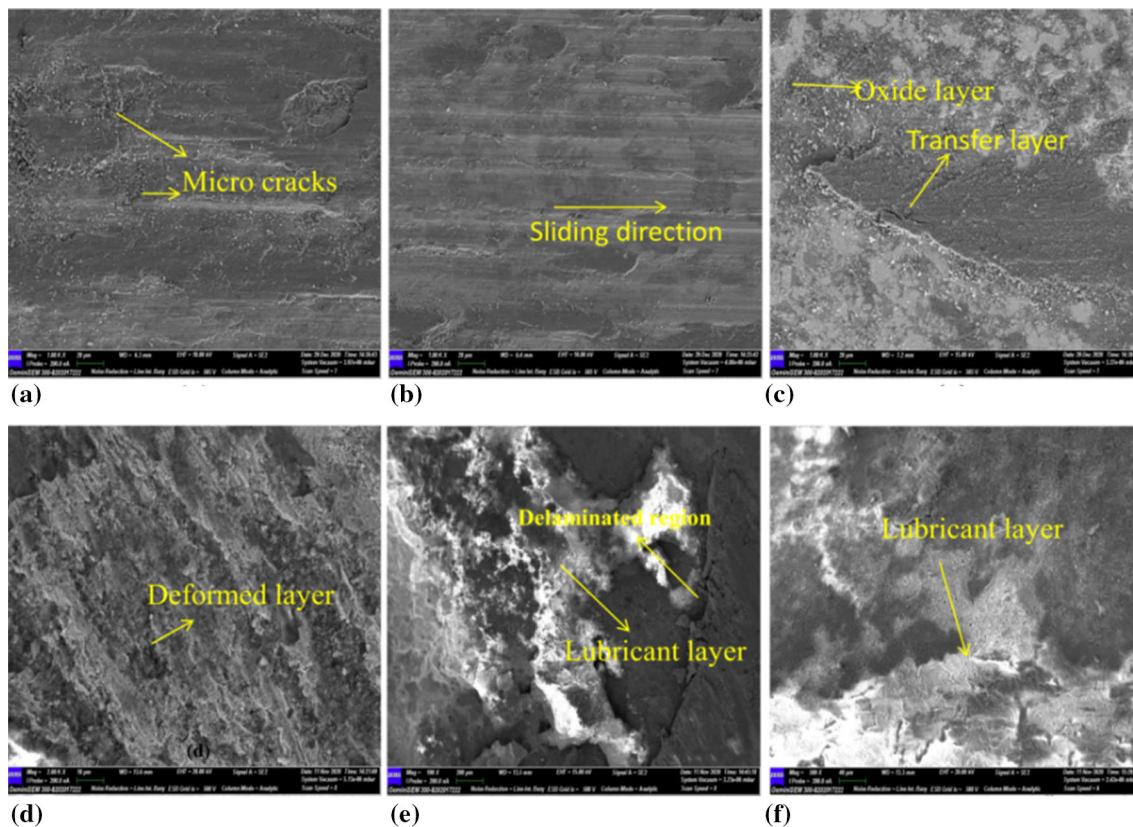


Fig. 15 SEM images of wear scars under 20 N load for (a) coating A at 200 °C, (b) 400 °C, (c) 600 °C, (d) coating B at 200 °C, (e) 400 °C, and (f) 600 °C

the load was 20 N. Figure 14 shows the coefficient of frictions of the Titanium 31 substrate, coating A, and coating B at 200 °C and 600 °C. The reduction of relative humidity because of the temperature rise in the contact areas resulted in a low coefficient of friction at the start of the test (Ref 38, 39). The average coefficient of friction of coating A was higher than those of the titanium 31 substrate and coating B. The high ceramic inclusion was detrimental to the coefficient of friction. The addition of solid lubricants helped reduce the material loss and coefficient of friction. At 20N load, the average coefficient of friction of coating B at 200 °C, 400°C, 600 °C is 0.375, 0.358, and 0.291, respectively. As increasing load to 40N, the average friction coefficient at 200 °C, 400 °C, 600 °C is 0.439, 0.397, and 0.338, respectively. A significant reduction in the coefficient of friction was observed, which could be attributed to the increase in the temperature due to the formation of the tribo layer. The Ag solid lubricant used in the coating led to the generation of low friction at the starting stages of the test. The use of the high-temperature solid lubricant BaF₂ resulted in reduced friction and weight loss at 600 °C. As the temperature rises from 200 to 600 °C, the coefficient of friction of coating A decreases (0.531-0.462), possibly due to the coating softening, resulting in a smooth surface. The uncertainty in the variation in the wear rate of the coatings was high. The degree of uncertainty depends on several factors such as defects, amount of wear debris on the track, and surface roughness. These can affect the wear rate calculation. The wear rates of coating A under 20 N loads at 200 °C, 400 °C, and 600 °C are 5.72×10^{-3} , 5.85×10^{-3} , and 5.23×10^{-3} mm³/N-m respectively. At 40 N load, wear rates at 200 °C, 400 °C, and 600 °C are

noted as 6.12×10^{-3} , 6.40×10^{-3} , and 6.92×10^{-3} mm³/N-m, respectively. Similarly, the wear rates of coating B at 200 °C, 400 °C, and 600 °C under 20 N load are 2.87×10^{-3} , 2.65×10^{-3} , and 2.27×10^{-3} mm³/N-m, respectively. As increasing load to 40 N, wear rates are noted at 200 °C, 400 °C, and 600 °C are 5.98×10^{-3} , 4.1×10^{-3} , and 3.2×10^{-3} mm³/N-m, respectively. Compared with the weight loss and wear rate for coating A, coating B exhibited superior wear performance, indicating its effective lubricant film formation ability.

3.5 Worn Surface Morphology

Figure 15 depicts the worn surfaces of coating A and coating B under the load of 20 N at different test temperatures. The degree of delamination observed for coating A at 600 °C was high. In the sliding wear operation, normal and shear stresses stimulate micro bulges on the surface to fracture (Ref 40). The removal of material takes place after the crack reaches a critical length. In Fig. 15(a, b, and c), the WC particles were pulled out because of abrasion against the alumina disk. This wear regime could be attributed to the surface fatigue that causes plastic shearing against the counter body. The formation of oxide on coating A helped reduce the degree of delamination at 600 °C. In coating B, deformation of the layer was observed at lower temperatures. The solid lubricant Ag can be effectively used for lubrication up to 400 °C (Ref 41). BaF₂ can provide lubrication above 450 °C (Ref 42, 43).

Figure 16(a, b, and c) shows the formation of deeper grooves and a higher degree of deformation of the coating. The pullout debris particles from the counter body can potentially act as third bodies at higher loads causing deeper grooves and

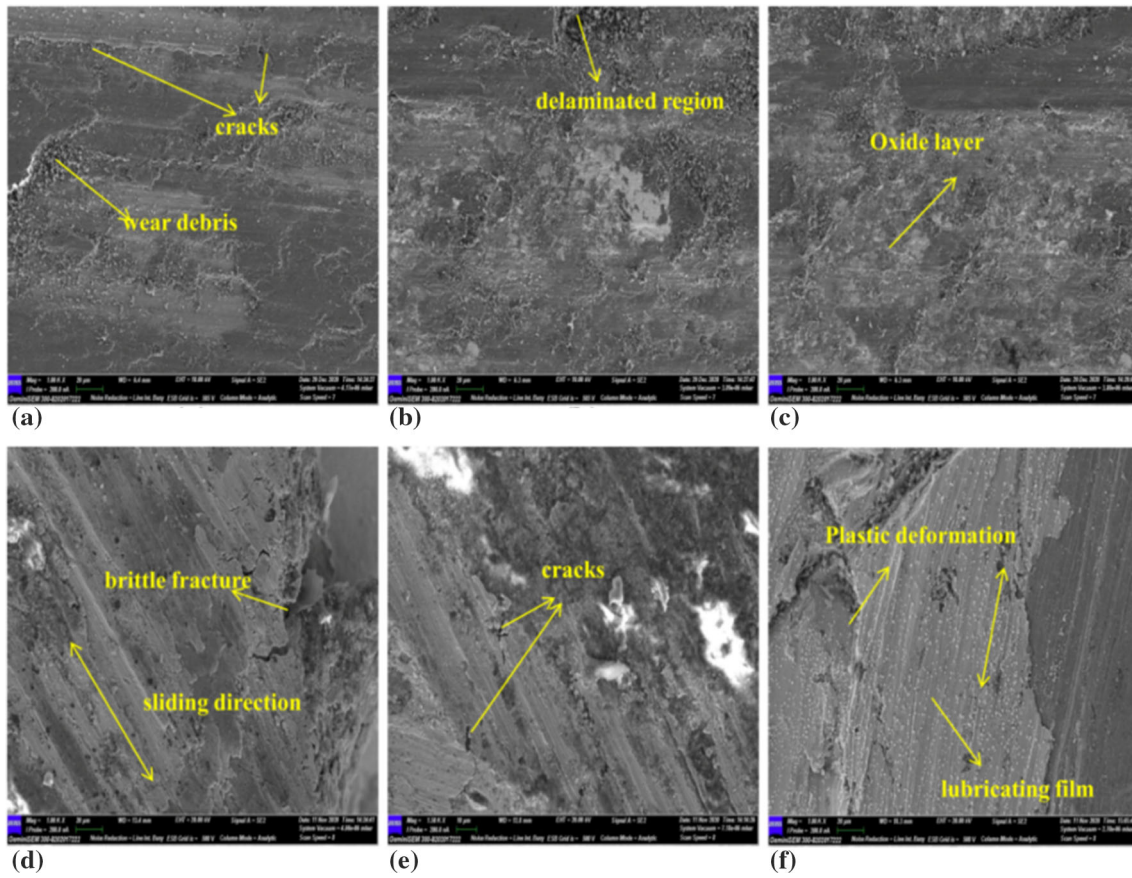


Fig. 16 SEM images of wear scars under 40N load for (a) coating A at 200 °C, (b) 400 °C, (c) 600 °C, (d) coating B at 200 °C, (e) 400 °C, and (f) 600 °C

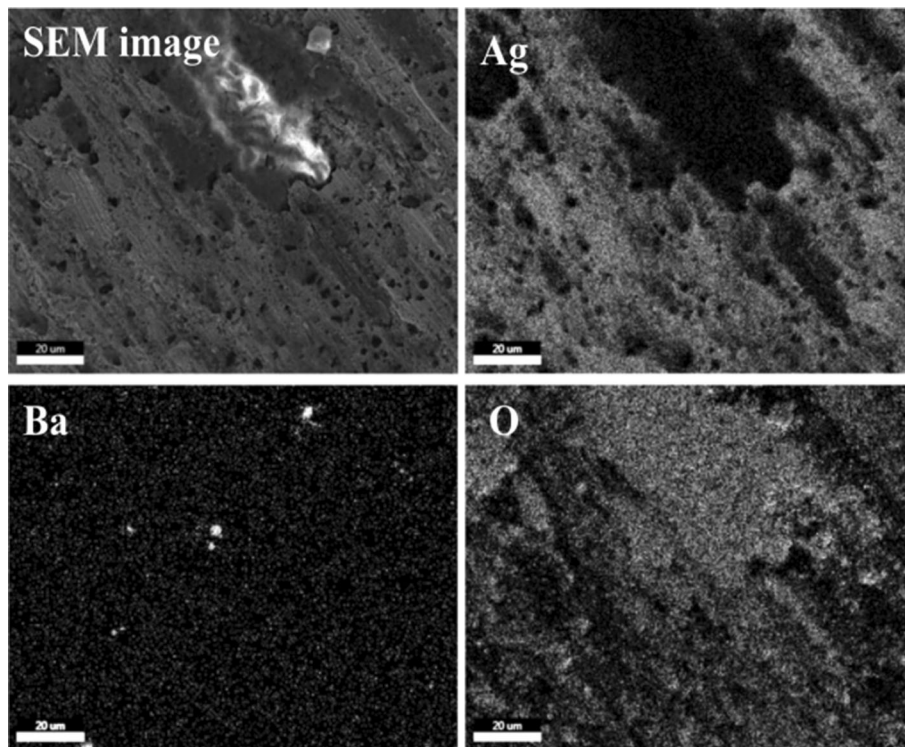


Fig. 17 EDX elemental mapping of the worn surface of coating B at 200 °C (load: 20 N)

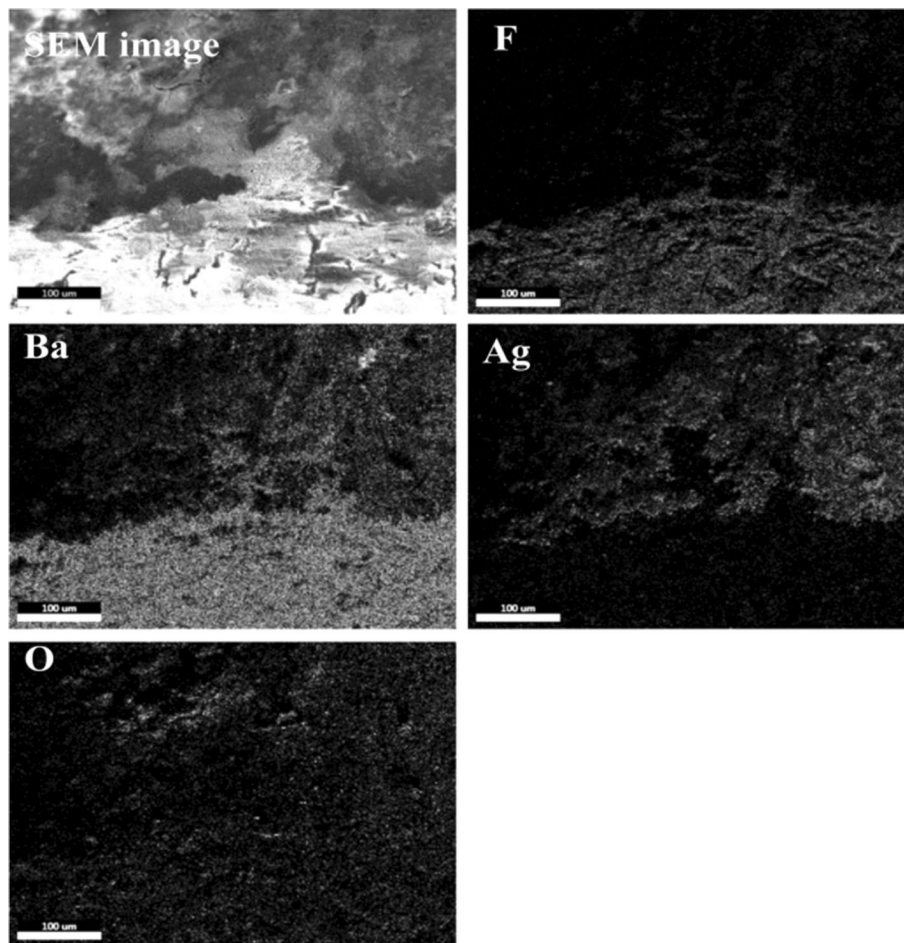


Fig. 18 EDX elemental mapping of worn surface of coating B at 600 °C (load: 20 N)

scratches. Apparent damage was observed when the load was 40 N. The Ag forms the lubricant layer at these test temperatures, but the extent of lubrication could not control coating delamination at higher loading conditions (40 N). As the test temperature increased, delamination of the coating reduced, as shown in Fig. 16(d, e, and f). At 200 °C, the elements Ag, O, and few amounts of F were detected on the surface using the EDX elemental mapping technique (shown in Fig. 17). The results revealed that Ba was ineffective in this temperature range. The formation of the Ag lubricant layer, intermetallic phase of NiTi, and other oxide phases helped reduce the formation of deep scratches and grooves. The EDX elemental mapping technique was used to characterize the worn surface of coating B at 600 °C (Fig. 18). A high content of Ba and F was observed on the worn surface. BaF₂ and the Ag phase were found to be effective in providing lubrication in the temperature range of 400–600 °C. The use of the combination of the solid lubricant in the coating helped reduce wear at both low and high temperatures. The solid Ag lubricants and eutectic BaF₂/CaF₂ can be easily distributed on the worn surface at higher temperatures (range: 600 °C–800 °C) (Ref 44). The primary lubrication factors are the plastic deformability of silver and brittle-ductile transition of BaF₂ (Ref 45). The wear mechanism involved the adhesive wear pathway, and the transfer layer break down. At lower temperatures, the wearing of coating A occurred due to the combined adhesive–abrasive wear action and spalling. It has been observed that the lubricity

obtained from coating B at 600 °C was more protective against the breakdown of the transfer layer.

3.6 Phase Analysis of the Worn Surfaces

Figure 19 exhibits the phase analysis of the worn surface of coating A at 200 °C and 600 °C. The XRD technique was used to analyze the samples. The intensity of the peaks was higher for the worn surface of the coating, which can be attributed to frictional heating and high temperature (Ref 46). The oxides formed on the worn surface were NiO, TiO, Ni₃Ti₃O, and W₃O. Their peak intensity increased with increasing temperature. These oxides can reduce the metal-to-metal contact, which reduces the shear strength of the contact surface. This can further induce the reduction in the wear rate and coefficient of friction (Ref 8, 47, 48). The phase analysis of coating B is shown in Fig. 20. The diffraction peaks corresponding to Ag₂F and Ba(TiO₃) were observed on the worn surface of coating B. The sintering reactions and other oxidation properties were stronger at 600 °C. It led to the formation of a favorable glaze layer on the worn surface (Ref 49). The silver phases formed as a continuous lubricating film on the worn surface and mitigated the wear rate and coefficient of friction at both low and high temperatures. Barium titanium oxide (Ba(TiO₃)) acted as an effective lubricant at high temperatures (600 °C). It could protect the coating from wearing out and helped in attaining a significantly low coefficient of friction (Ref 50). To sum up, the

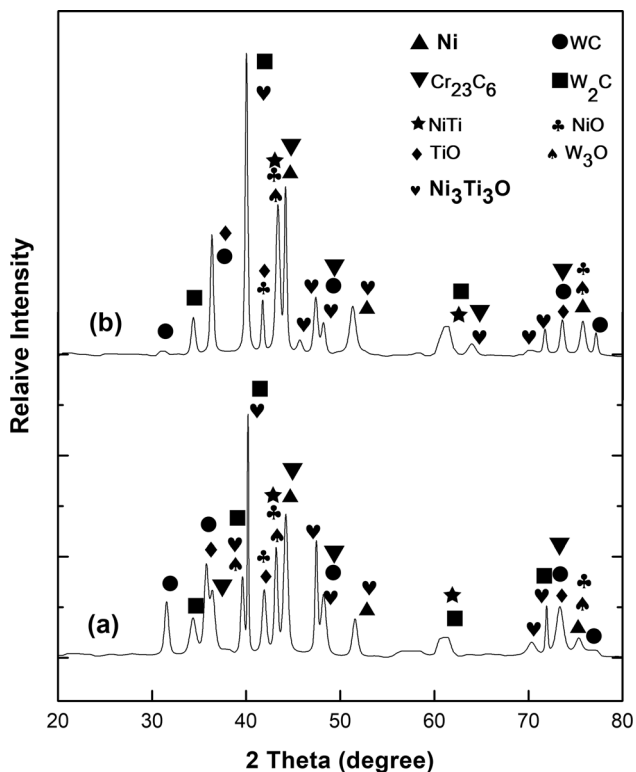


Fig. 19 XRD patterns of the worn surfaces of the coating A at (a) 600 °C and (b) 200 °C

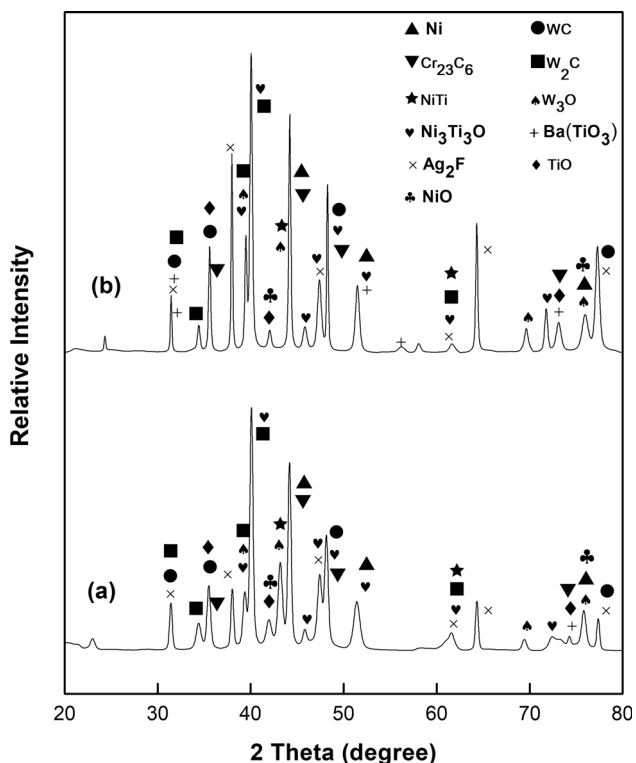


Fig. 20 XRD patterns of the worn surfaces of the coating B at (a) 200 °C and (b) 600 °C

tribo chemical reactions involving the solid lubricants and oxides on the worn surface of coating B were more efficient in

resisting wear than the reactions occurring on the surface of coating A at elevated temperatures.

4. Conclusions

Coatings NiCrSiB/WC (coating A) and NiCrSiB/WC/Ag/BaF₂ (coating B) exhibited good microstructural and mechanical properties when the process current was 70 A. The average hardness values of both the composite coatings were approximately four times higher than the average hardness of the titanium 31 substrate. The fracture toughness was evaluated, and the results indicated that the high ceramic phase exerted a negative effect on coating and induced brittle cracking under conditions of 2000 gf. The solid lubricant encapsulation in coating B leads to higher resistance to adhesive wear. The solid lubricants helped reduce material loss by providing lubrication throughout the temperature range. The hard intermetallic TiNi phase could prevent the formation of deep grooves and the extent of spalling. The oxide phases (NiO, Ni₃Ti₃O, W₃O) and lubricant phases (Ag, Ag₂F, and Ba(TiO₃)) helped reduce material loss. The wear resistance of coating B was approximately 20 times higher than that exhibited by the titanium 31 substrate and 3 times higher than coating A at 600 °C. This could be attributed to adequate lubricity at elevated temperatures.

References

1. P.F. Mendez, N. Barnes, K. Bell, S.D. Borle, S.S. Gajapati, S.D. Guest, H. Izadi, A.K. Gol and G. Wood, Welding Processes for Wear Resistant Overlays, *J. Manuf. Process.*, 2014, **16**(1), p 4–25.
2. D.E. Wolfe, J. Singh, J. Senderson and J. Zabinski, Laser-Clad Composite Coatings, *Adv. Mater. Process.*, 2000, **158**, p 41–44.
3. S. Buytoz, M. Ulutan and M.M. Yildirim, Dry Sliding Wear Behavior of TIG Welding Clad WC Composite Coatings, *Appl. Surf. Sci.*, 2005, **252**(5), p 1313–1323.
4. T. Liyanage, G. Fisher and A.P. Gerlich, Influence of Alloy Chemistry on Microstructure and Properties in NiCrBSi Overlay Coatings Deposited by Plasma Transferred Arc Welding (PTAW), *Surf. Coatings Technol.*, 2010, **205**(3), p 759–765. <https://doi.org/10.1016/j.surfcoat.2010.07.095>
5. M.R. Ramesh, S. Prakash, S.K. Nath, P.K. Sapra and B. Venkataraman, Solid Particle Erosion of HVOF Sprayed WC-Co/NiCrFeSiB Coatings, *Wear*, 2010, **269**(3–4), p 197–205. <https://doi.org/10.1016/j.wear.2010.03.019>
6. Z. Weng, A. Wang, X. Wu, Y. Wang and Z. Yang, Wear Resistance of Diode Laser-Clad Ni/WC Composite Coatings at Different Temperatures, *Surf. Coat. Technol.*, 2016, **304**, p 283–292. <https://doi.org/10.1016/j.surfcoat.2016.06.081>
7. S. Zhou, Y. Huang, X. Zeng and Q. Hu, Microstructure Characteristics of Ni-Based WC Composite Coatings by Laser Induction Hybrid Rapid Cladding, *Mater. Sci. Eng. A*, 2008, **480**(1–2), p 564–572.
8. M. Sabzi, S.M. Dezfouli and S.M. Far, Deposition of Ni-Tungsten Carbide Nanocomposite Coating by TIG welding: Characterization and Control of Microstructure and Wear/Corrosion Responses, *Ceram. Int.*, 2018, **44**(18), p 22816–22829. <https://doi.org/10.1016/j.ceramint.2018.09.073>
9. X. Luo, J. Li and G.J. Li, Effect of NiCrBSi Content on Microstructural Evolution, Cracking Susceptibility and Wear Behaviors of Laser Cladding WC/Ni-NiCrBSi Composite Coatings, *J. Alloys Compd.*, 2015, **626**, p 102–111.
10. H. Yu Wang, D. Wen Zuo, Y. Li Sun, F. Xu, and D. Zhang, Microstructure of Nanometer Al₂O₃ Dispersion Strengthened Ni-Based High-Temperature Protective Coatings by Laser Cladding, *Trans. Nonferrous Met. Soc. China*, 2009, **19**(3), p 586–591.

11. V. Fallah, M. Alimardani, S.F. Corbin and A. Khajepour, Impact of Localized Surface Preheating on the Microstructure and Crack Formation in Laser Direct Deposition of Stellite 1 on AISI 4340 Steel, *Appl. Surf. Sci.*, 2010, **257**(5), p 1716–1723. <https://doi.org/10.1016/j.apsusc.2010.09.003>
12. X.J. Tian, S.Q. Zhang, A. Li and H.M. Wang, Effect of Annealing Temperature on the Notch Impact Toughness of a Laser Melting Deposited Titanium Alloy Ti-4Al-1.5Mn, *Mater. Sci. Eng. A*, 2010, **527**(7–8), p 1821–1827. <https://doi.org/10.1016/j.msea.2009.11.014>
13. F. Gustavsson and S. Jacobson, Diverse Mechanisms of Friction Induced Self-Organisation into a Low-Friction Material - An Overview of WS₂ Tribofilm Formation, *Tribol. Int.*, 2016, **101**, p 340–347. <https://doi.org/10.1016/j.triboint.2016.04.029>
14. X. Quan, M. Hu, X. Gao, Y. Fu, L. Weng, D. Wang, D. Jiang and J. Sun, Friction and Wear Performance of Dual Lubrication Systems Combining WS₂-MoS₂ Composite Film and Low Volatility Oils Under Vacuum Condition, *Tribol. Int.*, 2016, **99**, p 57–66. <https://doi.org/10.1016/j.triboint.2016.03.009>
15. T.F. Babuska, A. Pitenis, M. Jones, B.L. Nation, W.G. Sawyer and N. Argibay, Temperature Dependent Friction Behavior of PTFE and MoS₂, *Tribol. Lett.*, 2016, **63**, p 1–12
16. K. Jin, Z. Qiao, S. Zhu, J. Cheng, B. Yin and J. Yang, Friction and Wear Properties and Mechanism of Bronze-Cr-Ag Composites under Dry-Sliding Conditions, *Tribol. Int.*, 2016, **96**, p 132–140. <https://doi.org/10.1016/j.triboint.2015.12.031>
17. J. Li, Y. He, D. Xiong, Y. Qin, J. Chen and H. Zhu, Tribological Properties of Silver Coatings with Laser Surface Textured Nickel as Interlayer, *Tribol. Int.*, 2016, **100**, p 178–185. <https://doi.org/10.1016/j.triboint.2016.01.009>
18. S.M. Aouadi, Y. Paudel, B. Luster, S. Stadler, P. Kohli, C. Muratore, C. Hager and A.A. Voevodin, Adaptive Mo 2N/MoS₂/Ag Tribological Nanocomposite Coatings for Aerospace Applications, *Tribol. Lett.*, 2008, **29**(2), p 95–103.
19. M.E. Cura, X.W. Liu, U. Kanerva, S. Varjus, A. Kivioja, O. Söderberg and S.P. Hannula, Friction Behavior of Alumina/Molybdenum Composites and Formation of MoO₃-x Phase at 400 °C, *Tribol. Int.*, 2015, **87**, p 23–31. <https://doi.org/10.1016/j.triboint.2015.02.010>
20. H. Torres, T. Vuchkov, S. Slawik, C. Gachot, B. Prakash and M. Rodríguez, Ripoll, Self-Lubricating Laser Claddings for Reducing Friction and Wear from Room Temperature to 600 °C, *Wear*, 2018, **408–409**, p 22–33. <https://doi.org/10.1016/j.wear.2018.05.001>
21. C.K. Sahoo and M. Masanta, Microstructure and Tribological Behaviour of TiC-Ni-CaF₂ Composite Coating Produced by TIG Cladding Process, *J. Mater. Process. Technol.*, 2017, **243**, p 229–245. <https://doi.org/10.1016/j.jmatprotec.2016.12.028>
22. C. Huang, L. Du and W. Zhang, Effects of Solid Lubricant Content on the Microstructure and Properties of NiCr/Cr₃C₂-BaF₂-CaF₂ Composite Coatings, *J. Alloys Compd.*, 2009, **479**(1–2), p 777–784.
23. M. Doddamani, M. Mathapati and M.R. Ramesh, Microstructure and Tribological Behavior of Plasma Sprayed NiCrAlY/WC-Co/Cenosphere/Solid Lubricants Composite Coatings, *Surf. Coatings Technol.*, 2018, **354**, p 92–100. <https://doi.org/10.1016/j.surfcoat.2018.09.018>
24. A. Lipp, K.A. Schwetz and K. Hunold, Hexagonal Boron Nitride: Fabrication, Properties and Applications, *J. Eur. Ceram. Soc.*, 1989, **5**(1), p 3–9. [https://doi.org/10.1016/0955-2219\(89\)90003-4](https://doi.org/10.1016/0955-2219(89)90003-4)
25. Y. Kimura, T. Wakabayashi, K. Okada, T. Wada and H. Nishikawa, Boron Nitride as a Lubricant Additive, *Wear*, 1999, **232**(2), p 199–206. [https://doi.org/10.1016/S0043-1648\(99\)00146-5](https://doi.org/10.1016/S0043-1648(99)00146-5)
26. X.L. Lu, X.B. Liu, P.C. Yu, S.J. Qiao, Y.J. Zhai, M. Di Wang, Y. Chen and D. Xu, Synthesis and Characterization of Ni₆₀-HfN High Temperature Self-Lubricating Anti-Wear Composite Coatings on Ti6Al4V Alloy by Laser Cladding, *Opt. Laser Technol.*, 2016, **78**, p 87–94. <https://doi.org/10.1016/j.optlastec.2015.10.005>
27. T. Otani, Titanium Welding Technology, *Nippon Steel Tech. Rep.*, 2007, **95**, p 88–92.
28. A.E. Yaedu and A.S.C.M. D'Oliveira, Cobalt Based Alloy PTA Hardfacing on Different Substrate Steels, *Mater. Sci. Technol.*, 2005, **21**(4), p 459–466. <https://doi.org/10.1179/174328413X13789824293380>
29. A.G. Evans and T.R. Wilshaw, Quasi-Static Solid Particle Damage in Brittle Solids—I, *Obs. Anal. Implic. Acta Metall.*, 1976, **24**(10), p 939–956. [https://doi.org/10.1016/0001-6160\(76\)90042-0](https://doi.org/10.1016/0001-6160(76)90042-0)
30. P.R. Reinaldo and A.S.C.M. D'Oliveira, NiCrSiB Coatings Deposited by Plasma Transferred Arc on Different Steel Substrates, *J. Mater. Eng. Perform.*, 2013, **22**(2), p 590–597.
31. P. Wu, H.M. Du, X.L. Chen, Z.Q. Li, H.L. Bai and E.Y. Jiang, Influence of WC Particle Behavior on the Wear Resistance Properties of Ni-WC Composite Coatings, *Wear*, 2004, **257**(1–2), p 142–147.
32. S.J. Bull, A.M. Jones and A.R. McCabe, Residual Stress in Ion-Assisted Coatings, *Surf. Coat. Technol.*, 1992, **54–55**, p 173–179. [https://doi.org/10.1016/S0257-8972\(09\)90046-9](https://doi.org/10.1016/S0257-8972(09)90046-9)
33. H. Yan, P. Zhang, Z. Yu, Q. Lu, S. Yang and C. Li, Microstructure and Tribological Properties of Laser-Clad Ni-Cr/TiB₂ Composite Coatings on Copper with the Addition of CaF₂, *Surf. Coat. Technol.*, 2012, **206**(19–20), p 4046–4053. <https://doi.org/10.1016/j.surfcoat.2012.03.086>
34. S. Lu, J. Zhou, L. Wang and J. Liang, Effect of V and Cr Transition Layers on Microstructure and Mechanical Properties of Ni-Based Coating on Titanium Alloy Fabricated by Laser Cladding, *Surf. Coat. Technol.*, 2021, **405**, p 126734. <https://doi.org/10.1016/j.surfcoat.2020.126734>
35. X. Jiao, J. Wang, C. Wang, Z. Gong, X. Pang and S.M. Xiong, Effect of Laser Scanning Speed on Microstructure and Wear Properties of Ti5M Cladding Coating Fabricated by Laser Cladding Technology, *Opt. Lasers Eng.*, 2018, **110**, p 163–171. <https://doi.org/10.1016/j.optlaseng.2018.05.024>
36. Y. Chen, F. Lu, K. Zhang, P. Nie, S.R. Elmi Hosseini, K. Feng, Z. Li and P.K. Chu, Investigation of Dendritic Growth and Liquation Cracking in Laser Melting Deposited Inconel 718 at Different Laser Input Angles, *Mater. Des.*, 2016, **105**, p 133–141. <https://doi.org/10.1016/j.matdes.2016.05.034>
37. A. Öztürk, K.V. Ezirmik, K. Kazmanli, M. Ürgen, O.L. Eryilmaz and A. Erdemir, Comparative Tribological Behaviors of TiN{single Bond}, CrN{single Bond} and MoN{single Bond}Cu Nanocomposite Coatings, *Tribol. Int.*, 2008, **41**(1), p 49–59.
38. P.J. Blau, Elevated-Temperature Tribology of Metallic Materials, *Tribol. Int.*, 2010, **43**(7), p 1203–1208. <https://doi.org/10.1016/j.triboint.2010.01.003>
39. E. Badisch, G.A. Fontalvo, M. Stoiber and C. Mitterer, Tribological Behavior of PACVD TiN Coatings in the Temperature Range up to 500 °C, *Surf. Coatings Technol.*, 2003, **163–164**, p 585–590.
40. Q. Liu, T. He, W.Y. Guo, Y. Bai, Y.S. Ma, Z.D. Chang, H.B. Liu, Y.X. Zhou, F. Ding, Y.W. Sun, Z.F. Han and J.J. Tang, Tribological Behavior of SAPS Sprayed Al₂O₃-TiO₂ and NiCr-Cr₃C₂ Coatings under Severe Load Conditions, *Surf. Coatings Technol.*, 2018, **2019**(370), p 362–373.
41. W. Wang, Application of a High Temperature Self-Lubricating Composite Coating on Steam Turbine Components, *Surf. Coat. Technol.*, 2004, **177–178**, p 12–17.
42. S. Zhu, Q. Bi, J. Yang and W. Liu, Ni₃Al Matrix Composite with Lubricious Tungstate at High Temperatures, *Tribol. Lett.*, 2012, **45**(2), p 251–255.
43. I. Tudela, A.J. Cobley and Y. Zhang, Tribological Performance of Novel Nickel-Based Composite Coatings with Lubricant Particles, *Friction*, 2019, **7**(2), p 169–180.
44. X.B. Liu, X.J. Meng, H.Q. Liu, G.L. Shi, S.H. Wu, C.F. Sun, M. Di Wang and L.H. Qi, Development and Characterization of Laser Clad High Temperature Self-Lubricating Wear Resistant Composite Coatings on Ti-6Al-4V Alloy, *Mater. Des.*, 2014, **55**, p 404–409. <https://doi.org/10.1016/j.matdes.2013.09.038>
45. M. Niu, Q. Bi, J. Yang and W. Liu, Tribological Performance of a Ni₃Al Matrix Self-Lubricating Composite Coating Tested from 25 to 1000°C, *Surf. Coat. Technol.*, 2012, **206**(19–20), p 3938–3943. <https://doi.org/10.1016/j.surfcoat.2012.03.064>
46. M. Aristizabal, L.C. Ardila, F. Veiga, M. Arizmendi, J. Fernandez and J.M. Sánchez, Comparison of the Friction and Wear Behaviour of WC-Ni-Co-Cr and WC-Co Hardmetals in Contact with Steel at High Temperatures, *Wear*, 2012, **280–281**, p 15–21. <https://doi.org/10.1016/j.wear.2012.01.015>
47. S. Zhu, Q. Bi, J. Yang, W. Liu and Q. Xue, Ni₃Al Matrix High Temperature Self-Lubricating Composites, *Tribol. Int.*, 2011, **44**(4), p 445–453. <https://doi.org/10.1016/j.triboint.2010.11.016>
48. J. Zhen, F. Li, S. Zhu, J. Ma, Z. Qiao, W. Liu and J. Yang, Friction and Wear Behavior of Nickel-Alloy-Based High Temperature Self-Lubricating Composites Against Si₃N₄ and Inconel 718, *Tribol. Int.*, 2014, **75**, p 1–9. <https://doi.org/10.1016/j.triboint.2014.03.005>

49. I.A. Inman, S.R. Rose and P.K. Datta, Studies of High Temperature Sliding Wear of Metallic Dissimilar Interfaces II: Incoloy MA956 Versus Stellite 6, *Tribol. Int.*, 2006, **39**(11), p 1361–1375.
50. Y. Mao, J. Yan, L. Wang, W. Dong, Y. Jia, X. Hu and X. Wang, Formation and Properties of Bioactive Barium Titanate Coatings Produced by Plasma Electrolytic Oxidation, *Ceram. Int.*, 2018, **44**(11), p 12978–12986. <https://doi.org/10.1016/j.ceramint.2018.04.115>

Publisher's Note Springer Nature remains neutral with regard to jurisdictional claims in published maps and institutional affiliations.